21st Australasian Fluid Mechanics Conference
Adelaide, Australia
10-13 December 2018

An investigation of turbulence structures in smooth pulsatile pipe flows under a very-high pulsatile forcing frequency

G. Z. Cheng, T. O. Jelly, S. J. Illingworth and A. S. H. Ooi

Department of Mechanical Engineering, The University of Melbourne, Melbourne 3010, VIC, Australia

Abstract

In this paper, direct numerical simulation (DNS) is performed to investigate the effects of pulsatile streamwise pressure gradient on turbulent smooth cylindrical pipe flows at a friction Reynolds number of 180 and very-high pulsation frequencies. The present study focuses on phase-averaged Reynolds shear stress and quadrant analysis including probability density function (PDF) and joint probability density function (JPDF). One turbulent pipe flow with non-pulsatile condition and the other with a very high pulsating frequency ($\omega^+ = 0.043$) are numerically experimented respectively, where strong dependence with pulsation is observed on phase-averaged Reynolds shear stress. The observation is mainly attributed to an intensive phase dependence of the low-speed turbulence structures and the ejection events in the second quadrant of the Reynolds shear stress.

Introduction

Pulsatile pipe flow is widely encountered in physical systems and engineering applications. The flow configuration can be described as a steady flow field superimposed with harmonic oscillations [5, 10, 12]. For pulsatile fully-developed turbulent pipe flows, the flow structures are affected by the amplitude and frequency of the superimposed velocity pulsation [6]. In terms of the amplitude of the velocity pulsation, the flow condition can be classified into wave- and current-dominated turbulent pipe flows, based on the ratio of the centre-line velocity oscillation to the time-averaged centre-line velocity. In the current-dominated flows, which is the focus of this paper, the ratio is less than unity. The flow characteristics are weakly dependent on the pulsation amplitude while showing high dependence on the pulsation frequency ω [8].

Recent research observed that the pulsation frequency has a strong effect on how far the vorticity generated from the pulsatile viscous wave at the wall could penetrate into the flow [8]. Tardu et al. [9] defined this frequency in a form of $\omega^+ = \omega\nu/\overline{u}_\tau^2$, where $\overline{u}_\tau$ is the time-averaged friction velocity, ν is the kinematic viscosity, and intervals of $0.02 < \omega^+ < 0.04$ and $\omega^+ > 0.04$ are categorised high and very-high frequency regimes, respectively. For high and very-high frequencies, the propagation of that vorticity is confined in the viscous sublayer [4]. As a result, the turbulence quantities will be weakly dependent on the pulsation [6]. However, throughout current published papers, the difference between high and very-high frequency regimes is still ambiguous and remains to be clarified. Brereton & Hwang [1] conducted a range of experiments with $\omega^+ = 0.01, 0.02, 0.04$ and 0.08, and reported that the time-averaged pulsating streamwise mean velocity profiles and phase-averaged streamwise turbulence intensities at those frequencies were barely distinguishable. More recently, Papadopoulos & Vouros [6] systematically analysed pulsatile flows in high and very-high frequency regimes and observed that phase-averaged turbulence intensities asymptotically approached phase independence and showed no obvious difference to classify high and very-high pulsation frequencies. However, these previous studies focused on the time- and phase-averaged mean velocity profiles and phase-averaged turbulence intensities. In this paper, an analysis is carried out on the Reynolds shear stress to provide a fundamental explanation for the effects of pulsation on turbulence characteristics.

Aims

Our objective is to complement previous studies by analysing the effects of pulsatile flows on the phase-averaged Reynolds shear stress and the instantaneous turbulence structures. The following data will be presented: (i) Phase-averaged turbulence statistics corresponding to Reynolds shear stress; (ii) High-order statistics including quadrant analysis and probability density functions; (iii) The instantaneous turbulence structures.

Simulation Setup and Validation

Pulsatile flow is achieved by prescribing a time-dependent axial pressure gradient of the form

$$\Pi(t) = \Pi_0 (1 + A\sin(\omega t)) \tag{1}$$

where Π_0 is the constant mean streamwise pressure gradient and A and ω denote the amplitude and frequency, respectively. The oscillatory component of the pulsatile pressure gradient is defined here as $\widetilde{\Pi}(t) = \Pi_0 A \sin(\omega t)$.

For pulsating turbulent pipe flows, the resulting instantaneous velocity field, $\mathbf{u}$, can be decomposed as [7]

$$\mathbf{u}(\mathbf{x},t) = \bar{\mathbf{u}}(r) + \tilde{\mathbf{u}}(r,\phi(t)) + \mathbf{u}'(\mathbf{x},t) \tag{2}$$

where $\bar{\mathbf{u}}$ is the global mean velocity, $\tilde{\mathbf{u}}$ is the zero-mean periodic component and $\mathbf{u}'$ is the stochastic fluctuation. Temporal phase is defined here as $\phi(t) = 2\pi(t/T \mod 1)$, where $T = 2\pi/\omega$ is the pulsation period.

Aligned along cylindrical coordinate where $\mathbf{x} = (r,\theta,x)$, the global-mean and phase-averaging operators can be written as,

$$\bar{\mathbf{u}}(r) = \frac{1}{2\pi L T_{total}} \int_0^{T_{total}} \int_0^{2\pi} \int_0^{L} \mathbf{u}(\mathbf{x},t)\, dx\, d\theta\, dt \tag{3}$$

$$\langle \mathbf{u} \rangle (r,\phi(t)) = \frac{1}{2\pi L N} \sum_{n=0}^{N-1} \int_0^{2\pi} \int_0^{L} \mathbf{u}(\mathbf{x}, t+nT)\, dx\, d\theta \tag{4}$$

where $T_{total} = NT$ is the total sampling period, N is the number of complete periods and L is the pipe length. Throughout this document, inner-scaled variables are denoted by a superscript "+", e.g. $\omega^+ = \omega\nu/\overline{u}_\tau^2$. The centreline velocity ratio is defined as $a_{uc} = (\max\langle u \rangle_{cl} - \overline{u}_{cl})/\overline{u}_{cl}$ and is held constant at 0.63. The friction Reynolds number is defined as $Re_\tau = \overline{u}_\tau R/\nu$ and held constant at 180. The Reynolds shear stress is defined as $\langle u_x' u_r' \rangle = \langle (u_x - \langle u_x \rangle)(u_r - \langle u_r \rangle) \rangle$.

To aid the analysis of results, it is useful to introduce the concept of acceleration and deceleration based on the behaviour of the phase-averaged axial bulk velocity, $\langle u_b \rangle$. The variation of $\langle u_b \rangle$ is unit-normalised and shown in Figure 1, along with the oscillatory axial pressure gradient. Accelerating phases are defined on the range $0 < \phi < \pi$, whereas decelerating phases are defined

on the range $\pi < \phi < 2\pi$. It is found that for the frequency under consideration, the phase-averaged centre-line velocity $\langle u_c \rangle$ and phase-averaged bulk velocity $\langle u_b \rangle$ align on the same phase.

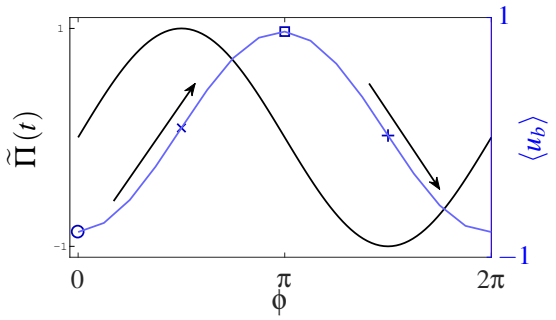

Figure 1: Schematic diagram of accelerating and decelerating phases. Phase dependence of oscillatory pressure gradient component $\widetilde{\Pi}(t)$ (—), and phase-averaged axial bulk velocity $\langle u_b \rangle$ at $\omega^+ = 0.043$ (—) are both unit-normalised and separated into acceleration ↗ and deceleration ↘. Four specific phases $\phi = \{0, \pi/2, \pi, 3\pi/2\}$ are presented $\{(\circ), (\times), (\square), (+)\}$.

In total, two numerical experiments were conducted, including one pulsatile case with forcing frequency $\omega^+ = 0.043$ and a non-pulsatile case for reference. Time integration was achieved using the PISO method [2] and based on the OpenFOAM library [3]. Spatial discretisation was based on a second-order accurate finite volume method. Impermeable no-slip boundary conditions were enforced on velocity, whereas Neumann boundary conditions were used for pressure. Periodic boundary conditions were enforced in the axial direction. A mesh consisting of hexahedra elements was used to resolve the pipe geometry with a pipe length of $2\pi D$, where the grid resolution at the wall and centreline are $\Delta_r^+ \approx 0.2, 4.71$ and $\Delta_x^+ \approx 5.89$, respectively.

In order to validate the accuracy of the current computational setup, recent results from Papadopoulos & Vouros [6] were reproduced. The phase-averaged mean velocity profile is shown in Figure 2 and the turbulence intensity profile is illustrated in Figure 3 at four different phases at $\omega^+ = 0.043$. Overall, good agreement between the two data sets is observed at all wall-normal locations for each phase.

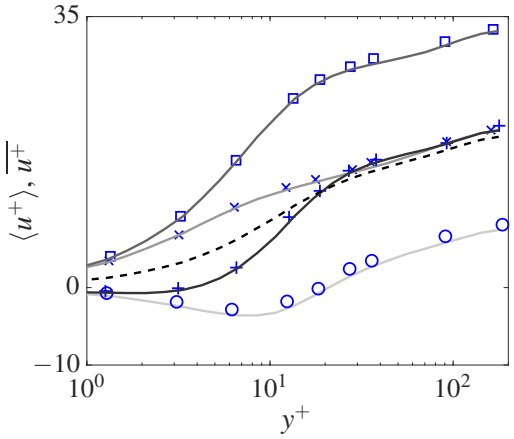

Figure 2: Phase-averaged mean velocity profile at four separate phases $\phi = \{0(—), \pi/2(—), \pi(—), 3\pi/2(—)\}$ along with Papadopoulos & Vouros [6] at each corresponding phase (refer to the symbols in Figure 1) and a non-pulsatile mean velocity profile (- - -).

Results

As was previously stated, the majority of past studies [6] have focused on phase-averaged profiles of axial velocity (Figure 2) and turbulence intensity (Figure 3). In order to complement previous work, in this study attention will be directed towards high-order phase-averaged turbulence statistics including: (i) Reynolds shear stress (RSS); (ii) quadrant decomposition of RSS and (iii) the joint probability density function (JPDF) of RSS. In addition, the instantaneous turbulence structures will be analysed. Herein, all results correspond to a forcing frequency of $\omega^+ = 0.043$ and a friction Reynolds number of $Re_\tau = 180$.

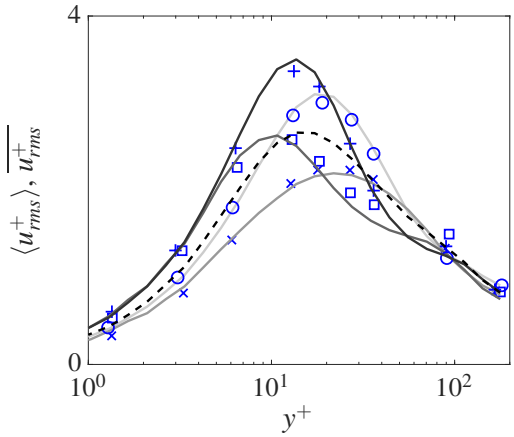

Figure 3: Phase-averaged axial turbulence intensity at four separate phases $\phi = \{0(—), \pi/2(—), \pi(—), 3\pi/2(—)\}$ along with Papadopoulos & Vouros [6] at each corresponding phase (refer to the symbols in Figure 1) and a non-pulsatile axial turbulence intensity (- - -).

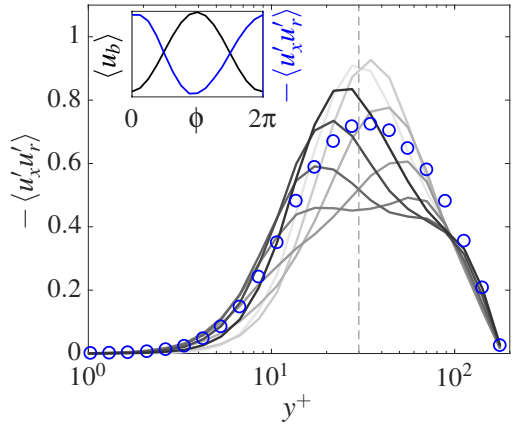

Figure 4: Phase-averaged Reynolds shear stress at eight separate phases $\phi = \{0(—), \pi/4(—), \pi/2(—), 3\pi/4(—)\}$, and $\{\pi(—), 5\pi/4(—), 3\pi/2(—), 7\pi/4(—)\}$. The most intensive modulation occurs at $y^+ = 30$ (- - -). Inset: Phase dependence of phase-averaged Reynolds shear stress $\langle u_x' u_r' \rangle$ (—) at $y^+ = 30$ and phase-averaged axial bulk velocity $\langle u_b \rangle$ (—).

Phase-averaged Reynolds Shear Stress

Profiles of the phase-averaged RSS, $\langle u_x' u_r' \rangle$, are shown in Figure 4. Unlike the phase-averaged mean velocity (Figure 2), the profiles of RSS exhibit two distinct behaviours. At phases on the interval $0 < \phi < \pi$, where the bulk flow is accelerating, the peak magnitude of $\langle u_x' u_r' \rangle$ decreases and moves towards the pipe

centreline. On the contrary, the peak magnitude of $\langle u'_x u'_r \rangle$ increases and moves towards the wall as the bulk flow decelerates — corresponding to the phases on the interval $\pi < \phi < 2\pi$. The strongest variation of $\langle u'_x u'_r \rangle$ with respect to phase is observed at $y^+ = 30$, which indicates the sensitivity of the near-wall cycle in this region.

In order to investigate the near-wall events associated with the behaviour of $\langle u'_x u'_r \rangle$ (Figure 4), a quadrant analysis was conducted. Following Wallace et al. [11], $\langle u'_x u'_r \rangle$ is decomposed into four quadrants: (i) outward interactions $Q_1\,(u'_x > 0, u'_r > 0)$; (ii) ejection events $Q_2\,(u'_x < 0, u'_r > 0)$; (iii) inward interactions $Q_3\,(u'_x < 0, u'_r < 0)$ and (iv) sweep events $Q_4\,(u'_x > 0, u'_r < 0)$. Out of the four quadrants, Q2 events exhibit the greatest sensitivity with respect to phase, and as a result, the following analysis focuses on the phase-averaged signature of ejection events. The joint probability density functions (JPDF) of Q2 events at $y^+ = 30$ are shown in Figure 5. As the bulk flow accelerates, the JPDF becomes narrower, indicating that it is less likely to observe high-amplitude low-probability axial velocity fluctuations. On the other hand, as the bulk flow decelerates, the JPDF widens and leads to an increased probability of high-amplitude events. Relative to axial velocity fluctuations, the JPDF of wall-normal velocity fluctuation u'_r shows a weak dependence on phase. Therefore, the remaining analysis focuses on further statistics of streamwise velocity fluctuations.

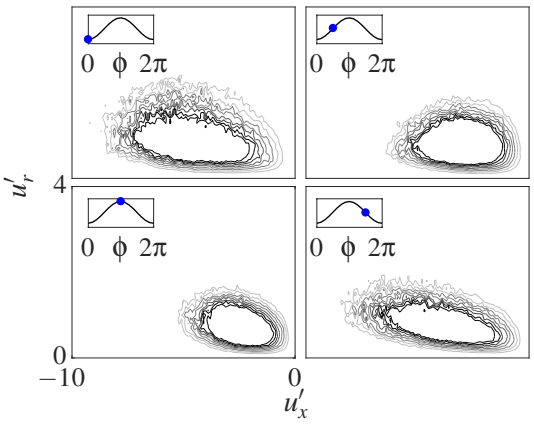

Figure 5: Quadrant analysis of JPDF weighted by u'_x and u'_r in Q_2 at each phase of $\langle u_b \rangle$, ϕ (•), in an entire period (refer to the inset (—)) of the harmonic pressure gradient at $y^+ = 30$.

Instantaneous Turbulence Structures

The probability density functions (PDF) of u'_x at $y^+ = 30$ under pulsatile and non-pulsatile conditions are compared in Figure 6. Overall, the pulsatile pressure gradient has a strong effect on the distribution of negative axial velocity fluctuations ($u'_x < 0$) — an observation consistent with the results shown previously in Figure 5. In contrast, the phase dependence of positive axial velocity fluctuations ($u'_x > 0$) is far weaker. As the bulk flow accelerates, the tails of the PDF of u'_x become shorter, indicating that the probability of high-magnitude fluctuations decreases. In contrast, both tails lengthen throughout the deceleration of the bulk flow.

The instantaneous turbulence structures in Figure 6 (right column) correspond to the PDF of u'_x at each phase. As the bulk flow is increasing ($0 < \phi < \pi$), narrowing $P\left(\tilde{u'_x}\right)$ on both tails indicates a reduction in the quantity of both low-speed streaks (LSS) and high-speed streaks (HSS), which implies that the difference between the turbulence structure scales is narrowing. On the contrary, as the bulk flow is decreasing ($\pi < \phi < 2\pi$), lengthening $P\left(\tilde{u'_x}\right)$ on both tails indicates an increase in the quantity of both LSS and HSS.

Conclusions

The current investigation reveals that at the threshold of very-high-frequency pulsation, Reynolds shear stress still shows a strong dependence on the pulsatile forcing frequency, where the dominant effect refers to the ejection events in the second quadrant of Reynolds shear stress and low-speed turbulence structures. Further systematical investigations on pulsatile turbulent pipe flow structures will be continued. Spectral analysis will be conducted in order to analyse the effects of pulsation on all turbulence length scales.

Themes

Turbulence, Boundary layers, Computaional fluid dynamics.

References

[1] Brereton, G. and Hwang, J.-L., The spacing of streaks in unsteady turbulent wall-bounded flow, *Phys. Fluids*, **6**, 1994, 2446–2454.

[2] Ferziger, J. H. and Peric, M., Computational methods for fluid mechanics, *Chapter*, **5**, 2002, 85–127.

[3] Greenshields, C. J., Openfoam user guide, *OpenFOAM Foundation Ltd, version*, **3**.

[4] He, S. and Jackson, J., An experimental study of pulsating turbulent flow in a pipe, *Eur. J. Mech. B/Fluids*, **28**, 2009, 309–320.

[5] Huang, R. F., Yang, T.-F. and Lan, Y.-K., Pulsatile flows and wall-shear stresses in models simulating normal and stenosed aortic arches, *Exp. Fluids*, **48**, 2010, 497–508.

[6] Papadopoulos, P. and Vouros, A., Pulsating turbulent pipe flow in the current dominated regime at high and very-high frequencies, *Int. J. Heat Fluid Flow*, **58**, 2016, 54–67.

[7] Reynolds, W. and Hussain, A., The mechanics of an organized wave in turbulent shear flow. part 3. theoretical models and comparisons with experiments, *J. Fluid Mech*, **54**, 1972, 263–288.

[8] Scotti, A. and Piomelli, U., Numerical simulation of pulsating turbulent channel flow, *Phys. Fluids*, **13**, 2001, 1367–1384.

[9] Tardu, S. F., Binder, G. and Blackwelder, R. F., Turbulent channel flow with large-amplitude velocity oscillations, *J. Fluid Mech*, **267**, 1994, 109–151.

[10] Varghese, S. S., Frankel, S. H. and Fischer, P. F., Direct numerical simulation of stenotic flows. part 2. pulsatile flow, *J. Fluid Mech*, **582**, 2007, 281–318.

[11] Wallace, J. M., Eckelmann, H. and Brodkey, R. S., The wall region in turbulent shear flow, *J. Fluid Mech*, **54**, 1972, 39–48.

[12] Xiao, B. and Zhang, Y., Numerical simulation of pulsatile turbulent flow in tapering stenosed arteries, *Int. J. Numer Method H*, **19**, 2009, 561–573.

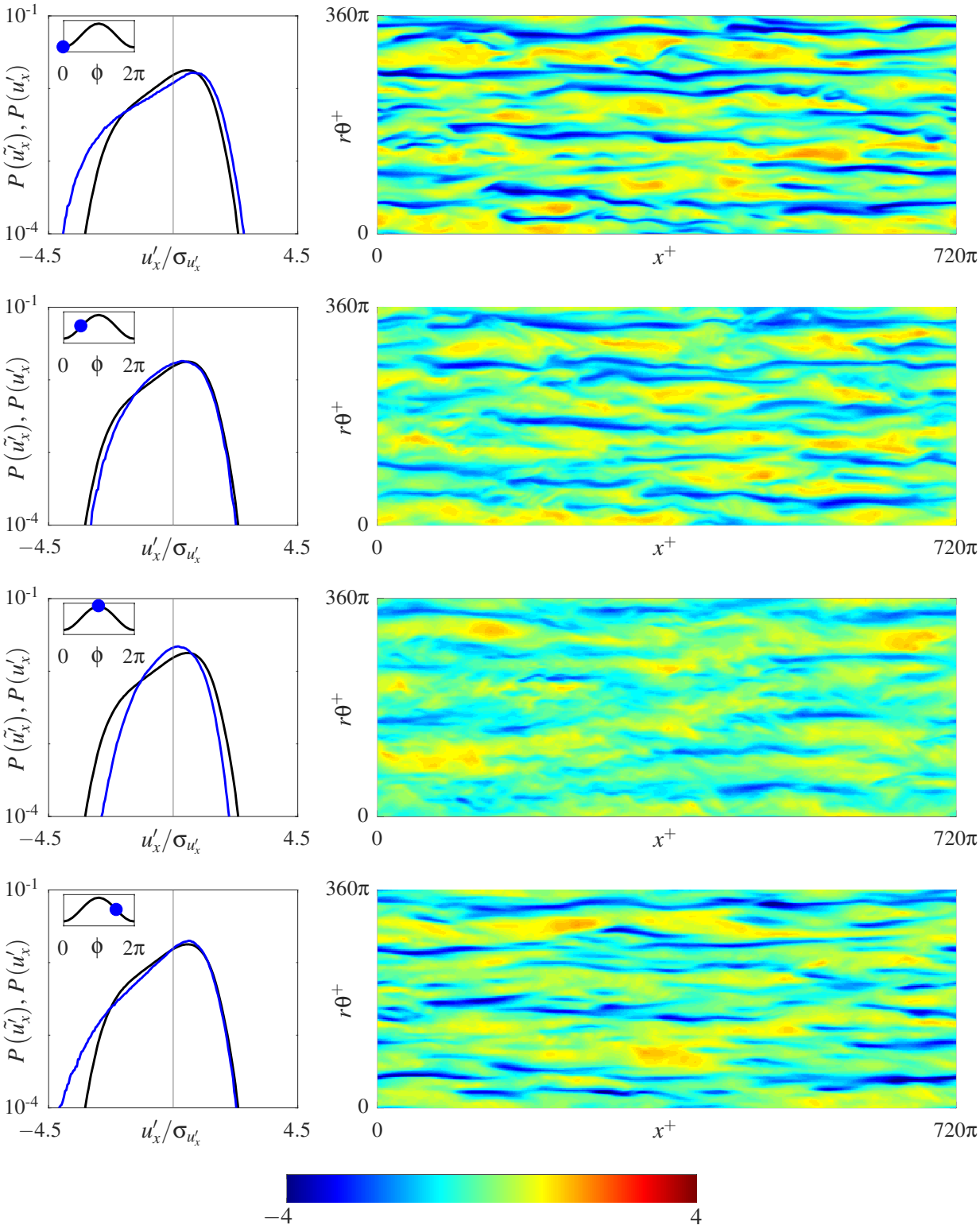

Figure 6: Left column: Comparison of the PDF of both pulsatile (—) and non-pulsatile (—) u'_x normalised by the standard deviation of non-pulsatile pipe flow $\sigma_{u'_x}$ at each phase of $\langle u_b \rangle$ (refer to the inset) (•) in a entire period (—) of the harmonic pressure gradient at $y^+ = 30$. $P(\tilde{u}'_x)$ and $P(u'_x)$ respectively denote the PDF of the pulsatile and non-pulsatile streamwise velocity fluctuations. Right column: The instantaneous $u'_x/\sigma_{u'_x}$ streaks referring to each reference phase of the PDF figures in the left column.